ACS APPLIED BIO MATERIALS

www.acsabm.org Article

Development of $CuAlO_2$-Encapsulated Reduced Graphene Oxide Nanocomposites: An Efficient and Selective Electrocatalyst for Detection of Neurodegenerative Disorders

Thirumalairajan Subramaniam,* Girija Kesavan, and Ganesh Venkatachalam

Cite This: https://dx.doi.org/10.1021/acsabm.0c00966 Read Online

ACCESS | Metrics & More | Article Recommendations | Supporting Information

ABSTRACT: Carbon-based nanomaterials continue to simulate wide interest in diverse disciplines including electrochemical biosensors, which have great ability to function as next-generation clinical diagnostics. Motivated by this point, we for the first time developed a $CuAlO_2$-encapsulated reduced graphene oxide (rGO) nanocomposite by a facile wet-chemical process to modify a glassy carbon electrode for dopamine detection with high selectivity and good sensitivity. The size, shape, phase purity, chemical composition, and surface area were investigated for the samples through transmission electron microscopy, scanning electron microscopy, high-resolution transmission electron microscopy, X-ray photoelectron spectroscopy, X-ray diffraction, and Brunauer–Emmett–Teller analysis. The electrocatalytic performance was studied using cyclic voltammetry and amperometric technique. The modified rGO/$CuAlO_2$ nanocomposite electrode showed an enhanced electrochemical performance compared to other electrodes and pure $CuAlO_2$ electrodes due to the strong promoting effect between rGO and $CuAlO_2$. Both the oxidation current and concentration were proportional and show a linear range of 9.2×10^{-8} to 1.6×10^{-7} M having a detection limit of 15 nM at S/N = 3. Further, the biosensor successfully neglected the interference of ascorbic and uric acid and exhibited enhanced selectivity, improved sensitivity, and stability toward dopamine formulations. Most obviously, the real-time analysis of the electrochemical biosensor may be proved using the clinical diagnostics in the near future.

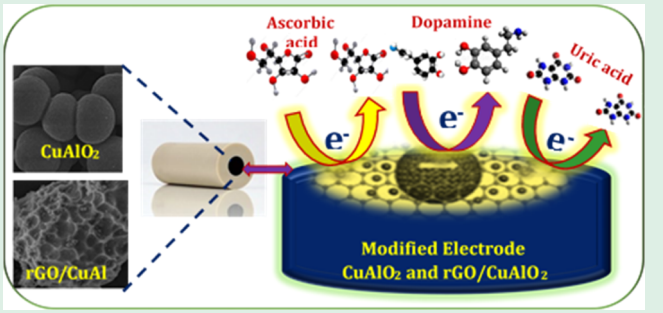

KEYWORDS: *rGO/$CuAlO_2$, electrochemical, biosensor, shape, size, dopamine*

1. INTRODUCTION

Neurotransmitters are the most significant messengers of the nervous system, and any deviation in their activities and balances can cause serious neurological, psychiatric, and cognitive disorders.[1,2] Among them, neurological disorders such as depression, schizophrenia, stress-related disease, and addiction are caused because of the abnormal function of the dopaminergic system.[3] Dopamine (DA) occurs in the highest amounts of 50 nmol g^{-1} in the portion of the human brain called caudate nucleus. However, DA occurs in low concentrations for a healthy individual, and it completely becomes null for persons affected with neurological disorders, especially, Parkinson's disease.[4] Detection of DA has been most favorably accomplished using electrochemistry with the ultimate task being the existence of high sensitivity and good selectivity toward DA detection. Several technologies including electrochemistry, chemiluminescence, spectrophotometry, and so forth have been used to detect DA.[5−8] These were designed for *in vivo* observation of DA at its physiological equivalent levels of 900−600 nM in Parkinson's patients medicated with L-dopa, and in the human brain, it changes in the range of 100 nM to 1 μM on DA release.[9−12] However, the release of DA and the following changes all happen in less than a few seconds, and hence the small changes in the concentration can be misestimated due to time-based resolution of these methods.[13]

Electrochemical biosensor-modified electrode can sense DA from the cerebral system at the nanomole level.[14−17] However, these biosensors have poor selectivity toward DA as these were designed with no recognition unit or molecular recognition. Ascorbic acid (AA), uric acid (UA), and DA have similar oxidation potentials, and hence discrimination of DA from AA and UA remains a challenge.[18] In the detection of DA, poor selectivity and sensitivity occurs as the surface of the electrodes is fouled by the products obtained during AA and UA oxidation.[19] This can be improved by choosing an appropriate

Received: August 3, 2020
Accepted: October 14, 2020

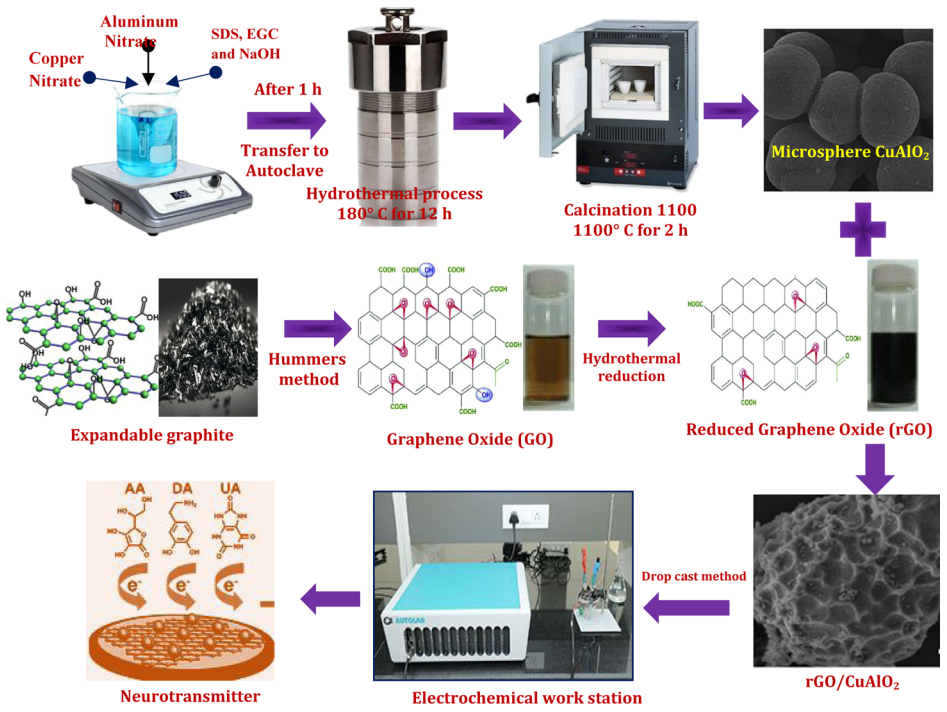

Figure 1. Systematic steps in the synthesis procedure of GO, $CuAlO_2$, and rGO/$CuAlO_2$ nanocomposite and their electrochemical detection toward neurotransmitter compounds.

material for the transducer matrix.[20,21] Reduced graphene oxide (rGO) with a thin sheetlike architecture and a high surface area is the material that has been used in the recent biosensor. It facilitates electron transfer and biomolecular affinity.[22] The features of the biosensor can be enhanced by incorporating metal and transition-metal oxides in rGO, which results in the variation of oxygen functional groups and defects.[23−25] Motivated by this point, delafossite $CuAlO_2$ structure, one of the transparent conducting oxide materials belonging to quasi-two-dimensional systems and markedly anisotropic, is a potential high surface area candidate for higher end biological applications because of its good catalytic activity and biocompatibility.[26−29] However, controlling the shape of graphene-based nanomaterials remains a challenge. Hence, further perfection of biosensing performance such as enhanced selectivity, improved sensitivity, and stability of carbon-based nanomaterials is still in demand. To the best of our knowledge, the rGO/$CuAlO_2$-modified electrode shows a much improved electrochemical performance toward neurotransmitter compounds, which has not been explored in the reported articles.

Focusing all above points, we present here the rGO/$CuAlO_2$ nanocomposite with exceptional physicochemical properties toward electrochemical detection of DA. Moreover, the synergistic effect between the rGO and $CuAlO_2$ nanospheres causes DA high performance compared to pure $CuAlO_2$. It exposes an outperformed benchmark electrocatalyst toward the detection of DA with high selectivity, good sensitivity, low detection, linear range, and stability and successfully neglects the interference of UA and AA. We believe that the developed biosensor can be successfully used to determine DA in clinical diagnostics in the near future.

2. EXPERIMENTAL TECHNIQUE

2.1. Synthesis of GO, rGO, $CuAlO_2$, and rGO/$CuAlO_2$. Graphene oxide (GO) was synthesized according to modified Hummers method[30] with the help of an expandable graphite flake as a precursor material, as reported in our previous publications.[31] Analytical pure grade chemicals were used directly for the experiments. Separate experiments were employed for the synthesis of rGO, $CuAlO_2$, and rGO/$CuAlO_2$. In the first experiment, 3.2 mg of the obtained dry GO was dispersed in 50 mL of deionized water by ultrasonication for 3 h, resulting in a brown color graphene solution. Then, equimolar amounts of $Cu(NO_3)_2{\cdot}3H_2O$, $Al(NO_3)_2{\cdot}9H_2O$, and sodium dodecyl sulfate were dissolved in 45 mL of deionized water under stirring to form a light blue colored solution, which was added to the above solution. 2 g of NaOH and 3 mL of ethylene glycol were added as an additive which resulted in a homogeneous blue colored solution. One hour later, the prepared solution was fed into a 110 mL Teflon-lined stainless-steel autoclave maintained at 180 °C for 12 h. The obtained products were centrifuged, washed, and then dried in air at 80 °C overnight. At last, the powder was annealed at 1100 °C for 2 h to obtain rGO/$CuAlO_2$ samples and used for further characterization analysis as shown in Figure 1. In the second experiment, $CuAlO_2$ was synthesized without the addition of GO. In the third experiment, rGO was prepared without adding the staring materials and surfactants under the same conditions, except for the calcination temperature.

2.2. Material Characterization. The surface morphology and crystal phase of the synthesized materials were investigated by scanning electron microscopy (SEM, JSM F-100). Transmission electron microscopy (TEM) and high resolution TEM (HRTEM) analyses were performed using a Tecnai F20 microscope at an accelerated voltage of 200 kV. X-ray diffraction (XRD) was performed using a Rigaku diffractometer, model DMax-2500 PC, with Cu Kα1 radiation (K = 1.5406 Å) in the 2θ range from 10 to 80 °C. The Raman spectrum was obtained using a LabRAM HR 800 Raman microscope.

X-ray photoelectron spectroscopy (XPS) technique recorded the binding energies using a ESCA + Omicron UK XPS system with a Mg Kα source and a photon energy of 1486.6 eV. Nitrogen adsorption−desorption isotherms were obtained using Brunauer−Emmett−Teller analysis from a Micromeritics ASAP 2020 system. A conventional three-electrode cell with a modified glassy carbon electrode (GCE, 3 mm in diameter) as the working electrode, a saturated Ag/AgCl

https://dx.doi.org/10.1021/acsabm.0c00966
ACS Appl. Bio Mater. XXXX, XXX, XXX−XXX

reference electrode, and a platinum wire as the auxiliary electrode were used for electrochemical experiments performed using CH1660B workstations. The modified GCE was fabricated as reported in our previous publications.[19]

3. RESULTS AND DISCUSSION

3.1. Surface Morphology and Particle Size Analysis. The surface morphology of the obtained samples was investigated through SEM. From Figure 2a, we observed that

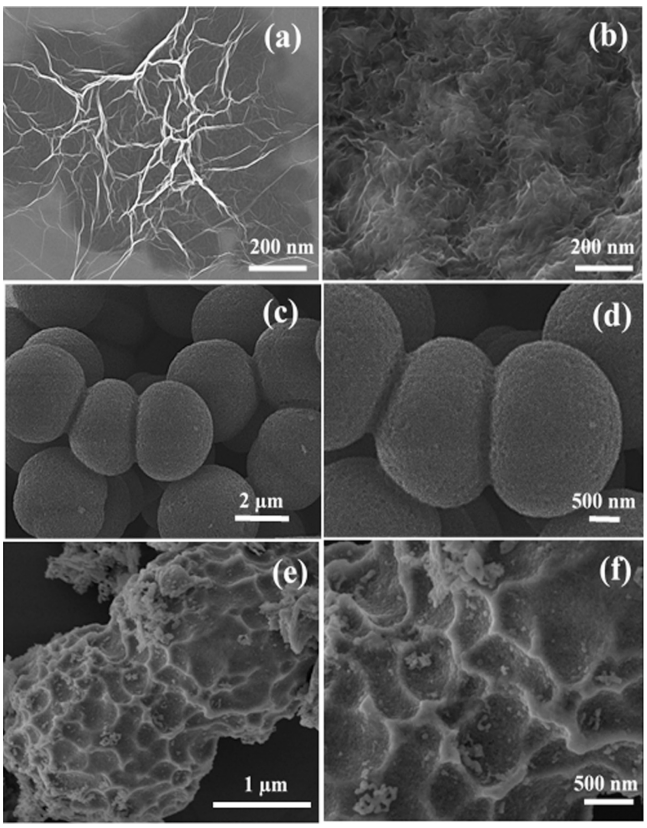

Figure 2. SEM images: (a) GO, (b) rGO, and (c,e) high-magnification and (d,f) low-magnification $CuAlO_2$ and rGO/$CuAlO_2$ nanocomposites.

interlinked three-dimensional porous platelet-like structures are formed. Figure 2b shows the rGO sheets obtained using the facile hydrothermal reaction without using any organic compounds. Overlap at the edges of wrinkled rGO can be observed, and it demonstrates the random accumulation of rGO sheets. Subsequently, we can observe low-magnification images of the $CuAlO_2$ sample in Figure 2c. The product has combined microspheres with diameters about 2.5 μm, and consequently from the close observation of Figure 2d, we can confirm that the microspheres are formed by numerous interconnected nanoparticles of average size ~60 nm. Amidst the interconnected particles, voids and interspaces can be located. The surfactant has a vital role in the construction of nanoparticles and assemblies from the single center, thereby acquiring the formation of the microsphere *via* a self-assembly process.[32] Figure 2e reveals that the $CuAlO_2$ microspheres encapsulated in rGO sheets are well organized having an average size approximately ~1.5 μm, which is smaller than that of pure $CuAlO_2$ microspheres, and the volume shrinks in the rGO sheet during the reaction time. This indicates that the reaction times, surfactant, and rGO concentration play a vital role in controlling the shape and size of the rGO/$CuAlO_2$ microspheres.[33] An enlarged image of the rGO/$CuAlO_2$ nanocomposite is shown in Figure 2f. rGO and $CuAlO_2$ are connected to each other, and the surface of $CuAlO_2$ microspheres exhibits a closely packed rGO with a hexagonal ordered arrangement. Based on our experiments, we believe rGO has a substantial part in the nucleation of the $CuAlO_2$ microspheres. The characteristic feature of rGO/$CuAlO_2$ is that the rGO sheets form a bridge between $CuAlO_2$ microspheres, which could significantly improve the sensing performance in the current work.

Further investigation into the morphology of $CuAlO_2$ nanostructure and rGO/$CuAlO_2$ nanocomposites was carried out using TEM and HRTEM analyses. Figure 3a presents the low-magnification TEM image taken from the combined $CuAlO_2$ microsphere with an average size of ~2.5 μm. From the high-magnification image of the $CuAlO_2$ microsphere (Figure 3b) (taken in the spot indicated by a circle in Figure 3a), it can be observed that each nanoparticle of the combined microsphere is distorted from a dense structure with a porous surface with interconnected nanoparticles of size *ca.* 60 nm.

Further information of the microsphere rGO/$CuAlO_2$ nanocomposites can be obtained from Figure 3d. The well-defined microspheres of ~1.5 μm diameter consist of small nanoparticles having average size *ca.* 40 nm, and also small foldings were present at the edges of rGO having only two layers of graphene, as seen in Figure 3e,f. We can distinctly view many minute projecting edges on the surface of the microsphere which is essentially composed of rGO nanosheets. The HRTEM images captured at the tip of the individual $CuAlO_2$ nanostructures and rGO/$CuAlO_2$ nanocomposites are presented in Figure 3c,f. It was noted that the crystallographic orientation of the particle was similar. Besides, the interlayer distance was 0.281 nm belonging to the (012) plane of $CuAlO_2$ microspheres, as presented in Figure 3c. The characteristic lattice fringes of $CuAlO_2$ microsphere in the surrounding of the rGO sheet can be seen in Figure 3f, with a *d*-spacing of 0.281 and 0.34 nm belonging to the planes (012) and (002) for $CuAlO_2$ and rGO. They were evaluated from randomly selected 50 fringes, as observed in Figure 3c,f. At the bottom (inset) of Figure 3c,f, the selected area electron diffraction (SAED) pattern of the samples is presented. The bright diffraction spots are indexed to the rhombohedral structure of $CuAlO_2$ with single-crystalline nature. The major diffraction spots correspond to (012), (006), and (101) planes. Diffraction spots belonging to the secondary or impurity phases were absent. The observed results of TEM and HRTEM go hand in hand with the SEM analysis.

3.2. Structural Analysis. Phase and structural purity of the prepared GO, rGO, $CuAlO_2$, and rGO/$CuAlO_2$ nanocomposite samples were analyzed by the powder XRD method. In Figure 4a, the XRD pattern of GO can be observed, and the strong peak at the (002) plane corresponding to a 2θ value at 10.79 has an interlayer spacing of 0.785 nm which is much higher than that of pristine graphite (0.34 nm).[33] The graphite surface contains a functional group belonging to the prefaces of oxygen which increases the interlayer spacing and also indicates the formation of GO by oxidation of expandable graphite.[34] Broadening and shifting of the XRD peak appear at 23.2 and 42.5°, which can be indexed to the (002) and (100) planes of graphene, and the restoration of C−C (sp^2) bonding confirms the conversion of GO to rGO after the hydrothermal

https://dx.doi.org/10.1021/acsabm.0c00966
ACS Appl. Bio Mater. XXXX, XXX, XXX−XXX

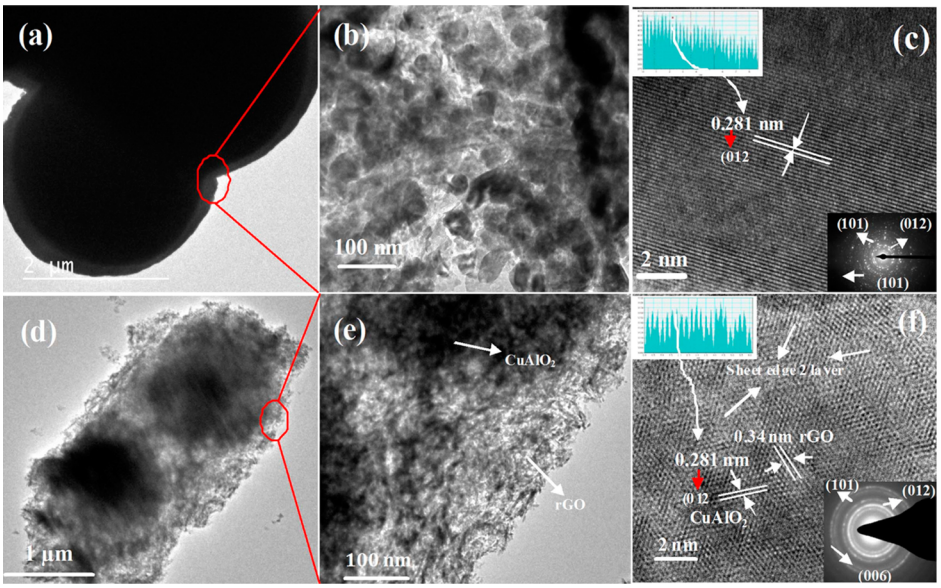

Figure 3. (a,d) Low magnification and (b,e) high magnification of TEM images. (c,f) HRTEM image of $CuAlO_2$ nanostructures and rGO/$CuAlO_2$ nanocomposites; (inset top) corresponding lattice interplanar spacing; (inset bottom) corresponding SAED pattern.

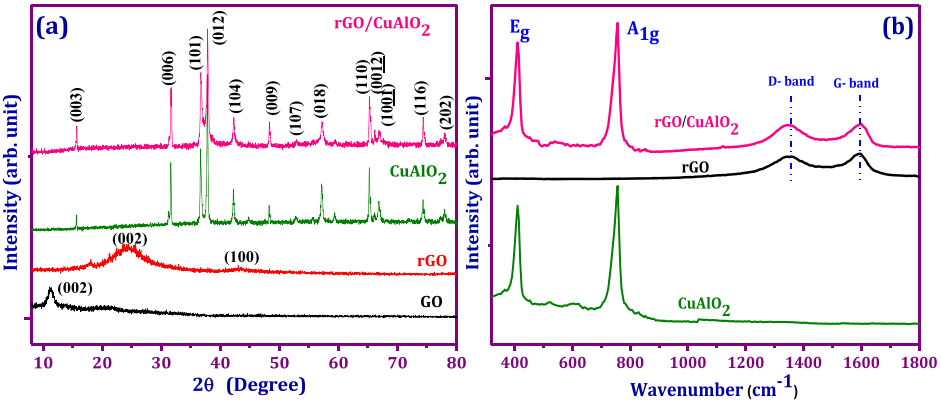

Figure 4. (a) XRD pattern and (b) Raman spectrum of GO, rGO, $CuAlO_2$, and rGO/$CuAlO_2$ nanocomposites.

treatment of GO. There were no noticeable changes between the XRD patterns of $CuAlO_2$ and rGO/$CuAlO_2$ nanocomposites, and all diffraction peaks belong to the single-phase $CuAlO_2$. The structural phase embraced is rhombohedral ($a = b = 2.8562$ Å, $c = 16.9584$ Å, within a maximum experimental error of ±0.0002, $\alpha = \beta = 90°$, $\gamma = 120°$).[35] The typical peaks related to impurity phases or belonging to rGO peaks were not detected in the XRD pattern of rGO/$CuAlO_2$ nanocomposites, which can be attributed to the low trace and small intensity of the rGO peak. Also, the rGO/$CuAlO_2$ nanocomposites display a small broad diffraction peak value compared to pure $CuAlO_2$, indicating higher oxygen functional groups on the GO surface along with carboxylic and hydroxyl groups to obstruct the diffusion and crystallization of $CuAlO_2$ grains. The observations of the XRD patterns confirm that $CuAlO_2$ microspheres were grown successfully on rGO by the wet-chemical process.

The average crystallite size was manipulated by the Debye–Scherrer formula[32] and was found to be ~65 and 42 nm for $CuAlO_2$ nanostructures and rGO/$CuAlO_2$ nanocomposites, respectively, which is almost related to observation from the particle size analysis.

Further, Raman spectroscopy was used as the sensitive technique to characterize layered materials to reveal the structure of rGO, $CuAlO_2$, and rGO/$CuAlO_2$ nanocomposites as shown in Figure 4b. As we can see, all prepared materials show a D band peak at around 1357 cm^{-1}, which occurs due to functional groups attached to the carbon basal plane. The G band peaks are observed at 1586 (rGO) and 1582 cm^{-1} (rGO/$CuAlO_2$). These can be attributed to the doubly-degenerated phonon mode (E_{2g} symmetry) occurring at the Brillouin zone center and to the in-plane vibrations of sp^2 carbon atoms.[36] It can also be because the hexagonal network of carbon atom with defects has been recovered by the "self-healing" characteristics of rGO, the presence of the D band peak, and the G band peak, which show a downshift from 1586 to 1582 cm^{-1}.[37] Also, a small increase in the I_D/I_G ratio was observed for the rGO/$CuAlO_2$ nanocomposites and was found to be 1.08. These focus points confirm the existence of new graphitic domains due to decrease in the sp^2 domain size of carbon atoms and the reduction of sp^3 to sp^2 carbon under the hydrothermal process. Further, the Raman spectra of rGO/$CuAlO_2$ nanocomposites are observed in the 200–800 cm^{-1} region, where the A_{1g} and degenerate E_g symmetries are Raman active modes that can be attributed to 417 and 765 cm^{-1}, same

https://dx.doi.org/10.1021/acsabm.0c00966
ACS Appl. Bio Mater. XXXX, XXX, XXX–XXX

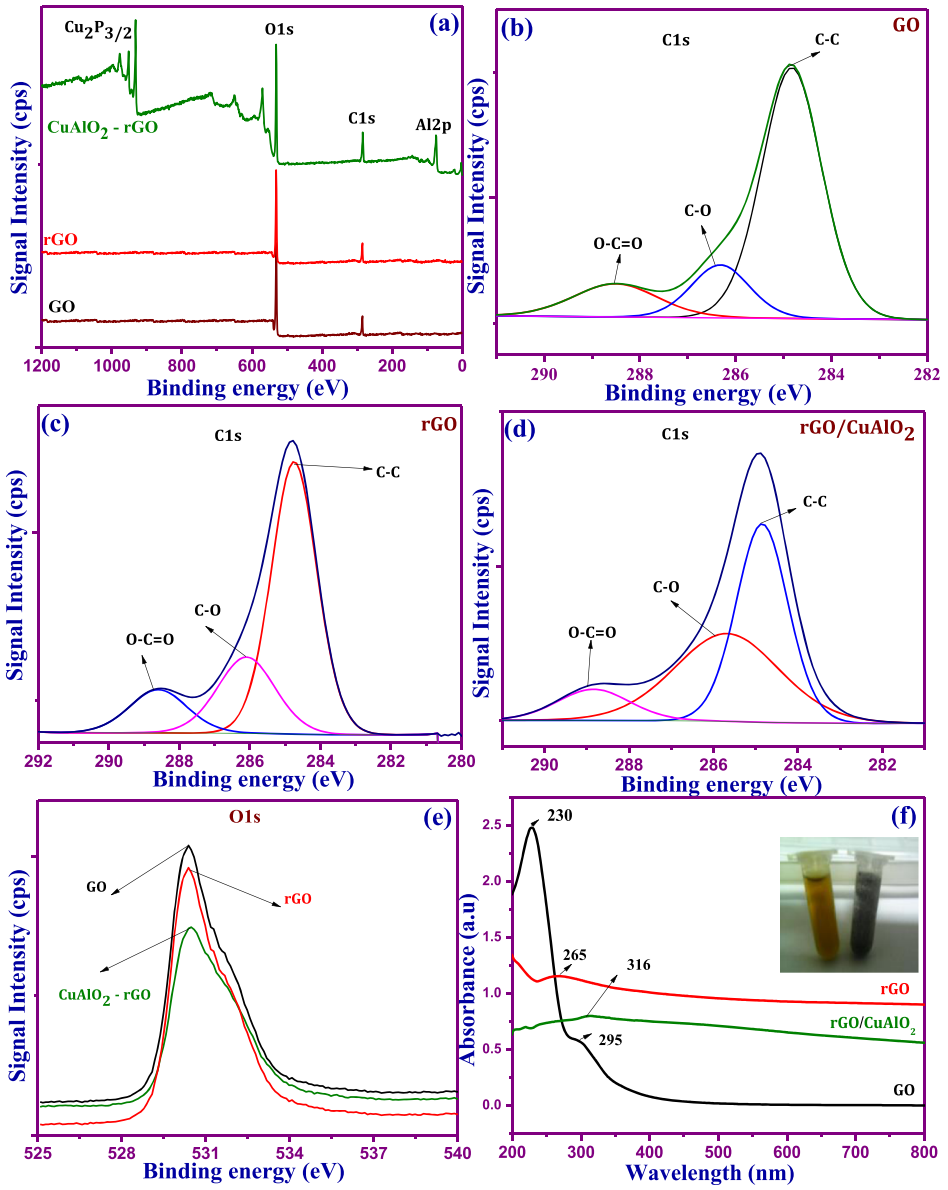

Figure 5. (a) XPS survey spectra, C 1s line after the offset of GO, rGO, and rGO/$CuAlO_2$ nanocomposites, (b–d) local fine scanning of O 1s of GO, $CuAlO_2$, and rGO/$CuAlO_2$ nanocomposites, and (f) UV–vis absorption spectra of GO, rGO, and rGO/$CuAlO_2$ nanocomposites.

as for $CuAlO_2$.[38] The A_{1g} and E_g modes were due to the vibrations of the Cu–O bond and perpendicular to the *c*-axis. The peak positions corresponding to the values are reported for $CuAlO_2$.[37] The as-prepared samples were of high purity as the peaks related to impurity and other phases were not detected. These results confirm that the prepared rGO/$CuAlO_2$ nanocomposites are a mixture of $CuAlO_2$ and rGO.

3.3. Chemical Composition Analysis. Further investigation of the chemical state of the synthesized samples was performed through the XPS technique. From the spectrum shown in Figure 5a, the elements Cu, Al, O, and C show their presence, and the survey spectra of GO, rGO, and rGO/$CuAlO_2$ nanocomposites confirm the presence of C 1s, Cu 2p, and 3p and also the related core levels Al 2p and O 1s. The C 1s spectrum of GO (Figure 5b) consists of the nonoxygenated C (284.5 eV), the carbon in C–O (286.7 eV), and the carboxylate carbon (O–C═O, 288.7 eV), in contrast in the rGO, the intensity of C–O and O–C═O peaks (Figure 5c). These results suggest that the oxygen-containing functional groups are completely removed after hydrothermal treatment. The reduction of peak intensities confirms the existence of residual oxygenate group in rGO. In rGO/$CuAlO_2$ (Figure 5d), the main broad peak at 284.3 eV and the peaks at 286.2 and 288.9 eV are attributed to the residual oxygen-containing groups. The observance of an oxygenated weaker peak suggests the deoxygenation of GO and the formation of rGO.[39] The enhancement in C–O ratio in rGO sheets can serve as a conductive channel between the $CuAlO_2$ microspheres and is favorable for the sensing process. The O 1s peak at 531.09, 531.24, and 531.35 eV for GO, rGO, and rGO/$CuAlO_2$ nanocomposites indicates the presence of chemisorbed O-containing species, attributed to the lattice oxygen as presented in Figure 5e.

The calculated C–O molar ratio shows the high content of oxygen species in GO (1:12.6), whereas the molar ratio was found to be only 1:3.18 for rGO, confirming the reduction of GO. On the other hand, the binding energy of Cu $2p_{3/2}$ and Cu $2p_{1/2}$ was found at 931.81 and 951.54 eV for the Cu^{2+} state,

https://dx.doi.org/10.1021/acsabm.0c00966
ACS Appl. Bio Mater. XXXX, XXX, XXX–XXX

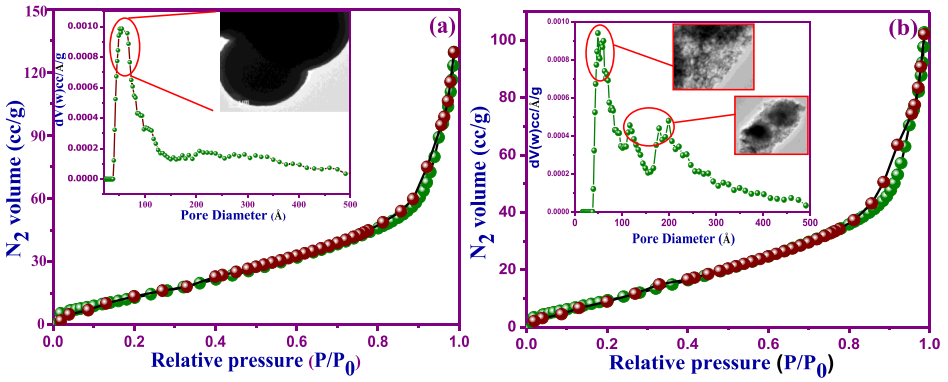

Figure 6. Nitrogen adsorption−desorption isotherms and the corresponding pore size distribution of (a) $CuAlO_2$ and (b) $rGO/CuAlO_2$ nanocomposites.

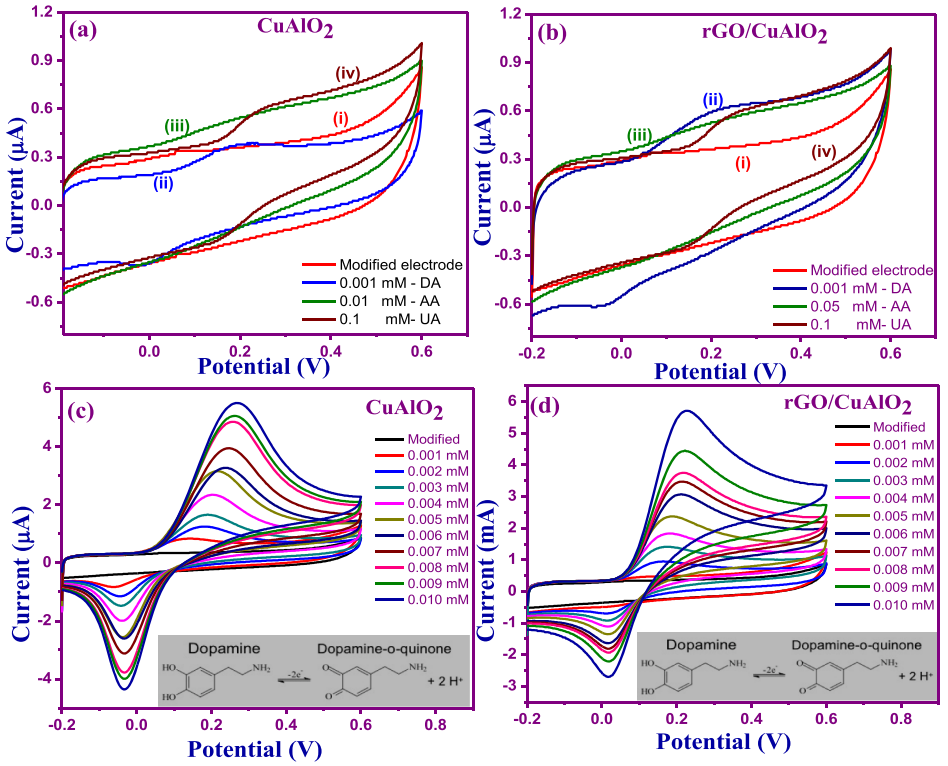

Figure 7. Cyclic voltammograms recorded in PBS (10 mM, pH 7.2) at 50 mV/s for the (a,c) modified electrode (brown); low concentration of DA (blue), high concentration of AA (green), and UA (brown) for $CuAlO_2$ nanostructures and $rGO/CuAlO_2$ nanocomposites. (b,d) Various concentrations (1−10 μM) of DA for $CuAlO_2$ nanostructures and $rGO/CuAlO_2$ nanocomposites.

which confirms that Cu in $CuAlO_2$ is in +1 state. The impurity phases of CuO and $CuAl_2O_4$ are not present because of annealing treatment in the prepared samples. The Al 2p peak of Al^{3+} at 74.20 and 74.24 eV and the Cu $3p_{1/2}$ peak at 78.60 of Cu^+ were also observed in the prepared samples[39] which can be attributed to the interaction between Cu 3p and Al 2p. It was confirmed that the Al element can exist in the form of $CuAlO_2$. All of the binding energy values of C, O, Cu, and Al infer the chemically bonded state of the elements. Compositional analysis along with the structural results indicate that the synthesized samples were GO, rGO, and $rGO/CuAlO_2$ composites. The XPS spectrum indicated that the $rGO/CuAlO_2$ nanocomposites have a higher ratio of oxygen vacancies than $CuAlO_2$ nanostructures, which could contribute to higher catalytic actives for potential applications.

As presented in the UV−vis spectrum, the reduction of GO by γ-ray irradiation was monitored using UV−vis analysis (Figure 5f). GO exhibits two bands, a maximum $\pi-\pi^*$ transition of aromatic C−C bond at 230 nm and a shoulder $n-\pi^*$ absorption band at 295 nm for the transition of C═O bonds, whereas the peak of $\pi-\pi^*$ transition shifts to 265 nm for rGO, representing that some groups on the GO surface could have been removed, and the conjugated structure was restored.[40,41] Besides, the GO solution turned to deep black after the γ-ray irradiation, which indicates the reduction of GO as shown in Figure 5f (inset). The sharp absorption peak at 316 nm of the $rGO/CuAlO_2$ nanocomposites obtained during irradiation indicates the crystalline nature and the modification of electron−hole pair.

3.4. Surface Area Analysis. Nitrogen physisorption measurements validated the surface area and porous nature

https://dx.doi.org/10.1021/acsabm.0c00966
ACS Appl. Bio Mater. XXXX, XXX, XXX−XXX

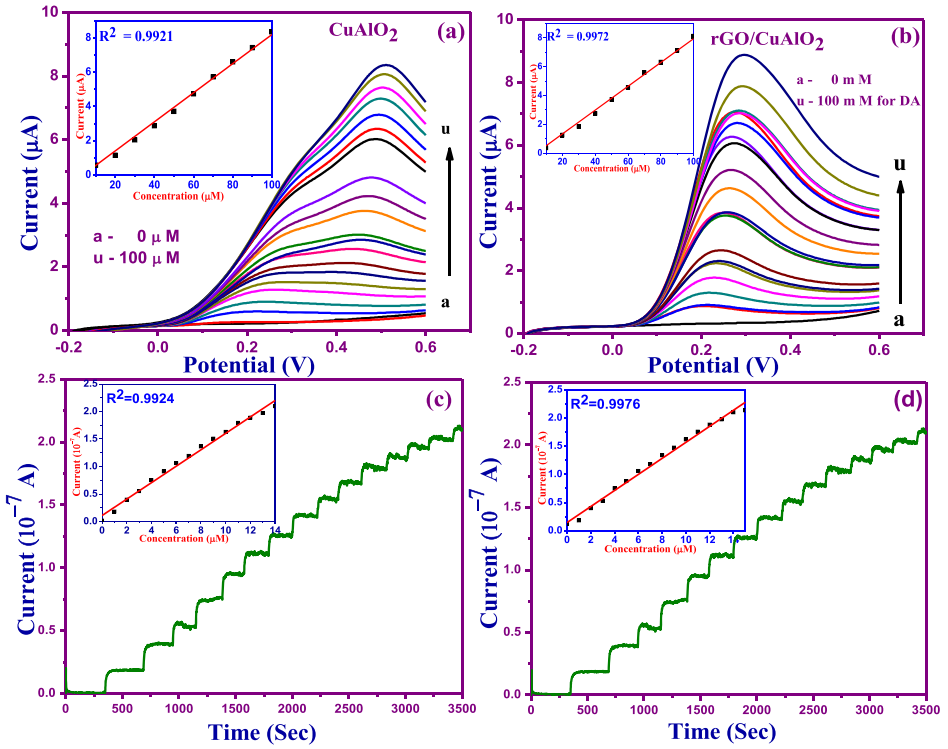

Figure 8. LSVs obtained for DA concentration range from 0 to 100 μM for (a) $CuAlO_2$ and (b) rGO/$CuAlO_2$ nanocomposites. (c,d) Amperometric $i-t$ curve for the determination of DA concentration by the $CuAlO_2$ nanostructure- and rGO/$CuAlO_2$ nanocomposite-modified electrodes (inset—current *vs* concentration for DA).

of $CuAlO_2$ nanostructures and rGO/$CuAlO_2$ nanocomposites. The absorption−desorption isotherm of both the samples represents the type IV, H3 hysteresis loop with pressure in the range $0.8 < P/P_0 < 1.0$, which typically represents mesopores with different pore sizes as presented in Figure 6a,b. The specific surface area of the $CuAlO_2$ microspheres is 65 $m^2\ g^{-1}$ with a pore volume of 0.12 $cm^3\ g^{-1}$, while for the rGO/$CuAlO_2$ nanocomposites, the specific surface area increases to 148 $m^2\ g^{-1}$ with a pore volume of 0.26 $cm^3\ g^{-1}$, which is from the rGO that has the adsorbing ability to the analyte during biosensing, which is beneficial to accomplish an enhanced biosensing performance, such as high selectivity, sensitivity, and low detection limit and has been discussed in a later section.

Furthermore, the pore volume curves represent the pore size distribution of $CuAlO_2$ microspheres and rGO/$CuAlO_2$ nanocomposites, which were evaluated using the Barrett−Joyner−Halenda model shown in the inset of Figure 6a,b. Microsphere $CuAlO_2$ nanostructures have a homogenous pore size of ∼2−5 nm. Subsequently, the pore size distribution curve of rGO/$CuAlO_2$ nanocomposites has two distinct peaks. The first peak located at ∼2 nm can be attributed to the small nanoparticles assembled to form microspheres. The presence of small nanoparticles in the rGO/$CuAlO_2$ composites with different sizes has been discussed in the Surface Morphology and Particle Size Analysis section. Moreover, the peak with pore diameter ∼10 nm represents the composite of $CuAlO_2$ and rGO sheet. The pores in the composites occur due to the interspace between rGO and $CuAlO_2$ nanostructures and also by the encapsulation of rGO and $CuAlO_2$. The large surface area and good pore volume of rGO/$CuAlO_2$ nanocomposites pave way for more exposed active sites and favor the mass transport of reactants and products for sensing performance. Therefore, the high crystallinity, shape, size, and large surface area help in obtaining an open porous structure, which facilitates the biosensing applications.

3.5. Electrocatalytic Effect of $CuAlO_2$ Nanostructure and rGO/$CuAlO_2$ Nanocomposites. From the scientific and technological understanding, it is essential to cultivate biosensors with good selectivity, sensitivity, and low detection of neurotransmitter compounds. Lately, advancements in the research and development of carbon-based nanostructures have progressively stressed the biosensor applications. Herein, $CuAlO_2$ nanostructure and rGO/$CuAlO_2$ nanocomposite-functionalized GCE for biosensing detection such as DA, AA, and UA have been reported. The electrochemical behavior of different modified electrodes such as $CuAlO_2$ nanostructure and rGO/$CuAlO_2$ nanocomposites in the presence of 10 mM phosphate-buffered saline (PBS, pH 7.2) was investigated by cyclic voltammetric (CV) curves at a scan rate of 50 mV/s in the fixed operating potential of −0.2 to 0.6 V. Figure 7a,b represents the CV response curves of (i) DA, AA, and UA, which show no reaction peaks for the modified GCE. Subsequently, $CuAlO_2$ nanostructure- and rGO/$CuAlO_2$ nanocomposite-modified electrodes revealed the quasi-reversible performance to 1 μM DA in pH 7.2 (Figure 7a,b, curve ii). DA oxidation and reduction peak potential separation (ΔE) was about 190 and 320 mV, while peak-to-peak separation values of AA (140 and 160 mV for 50, 100 μM) and UA (210 and 250 mV for 100 μM) were observed at the modified electrode of $CuAlO_2$ nanostructures and rGO/$CuAlO_2$ nanocomposites. At the surface of the functionalized electrode, the electron-transfer kinetics is not active, which can be attributed to nonconductive components and electrode entangling occurred by the deposition of AA and UA and their oxidation products on the surface of the electrode.[42,43] The

https://dx.doi.org/10.1021/acsabm.0c00966
ACS Appl. Bio Mater. XXXX, XXX, XXX−XXX

oxidations for DA, AA, and UA are positioned at 183, 198, and 229 mV for the modified rGO/$CuAlO_2$ nanocomposite electrode. The peak makings of DA−AA, UA−AA, and UA−DA with oxidation peak partings of 15, 31, and 46 mV, respectively, were observed. These partings are not adequate for the synchronized detection of these analytical compounds. It is determined that the detection of DA is as low as 50 and 100 times for AA and UA in the case of both modified electrodes. The rGO/$CuAlO_2$ nanocomposite electrode has excellent selectivity toward DA, which can be explained as follows.

Graphene plays the role of effective electron promotor for the electrocatalytic oxidation of DA. The interaction energy that occurs between graphene sheets and $CuAlO_2$ nanostructures increases the conductive area and electron-transfer rate between the electrode surface and applied biocompounds. DA quinone (DAQ), the oxidized product, and the reoxidation process have been studied, and the probable mechanism of the electrochemical performance of DA has been presented in Figure 7 (inset). DA is oxidized to DAQ after the exchange of two protons and two electrons, while a potential is supplied to the electrode.[44] From the results obtained, we can understand that the electrode functionalized with the rGO/$CuAlO_2$ nanocomposite was 1.3-fold higher than pure $CuAlO_2$ modified electrodes. These results confirm the good electrooxidation capability of the nanocomposite-modified electrode toward DA, which results from the synchronized activity of $CuAlO_2$ and rGO. The good conductivity of GO and the tremendous deoxidation capability of $CuAlO_2$ resulted in excellent oxidation with lower potential detection of DA. Hence, the sensitive rGO/$CuAlO_2$ nanocomposite biosensor can be involved in the detection of DA.

Further, the electrocatalytic properties of the $CuAlO_2$ nanostructure- and rGO/$CuAlO_2$ nanocomposite-modified electrodes at different concentrations for DA detection were obtained after additional examinations, as presented in Figure 7c,d. The electrocatalytic ability of the $CuAlO_2$ nanostructures and rGO/$CuAlO_2$ nanocomposites toward the reduction of DA concentrations (1−10 μM) in 10 mM PBS (pH = 7.2) at a scan rate of ∼50 mV/s was observed. The peak currents of DA are directly proportional to the DA concentration, and hence an increase in the DA concentration leads to an increase in the peak current. Linearity between the reaction of the electrode and the anodic peak current of the electrode with DA resulted due to a controlled diffusion process. These results infer that the $CuAlO_2$ nanostructure- and rGO/$CuAlO_2$ nanocomposite-functionalized electrodes have excellent electrochemical activity toward DA oxidation.

Figure 8a,b represents the linear sweep voltammogram (LSV) response of $CuAlO_2$ nanostructure- and rGO/$CuAlO_2$ nanocomposite-modified electrodes for various DA concentrations. Both the electrodes responded as the oxidation current of DA constantly increased with the increase in 5 μM concentration of DA within the range 0−100 μM. From the LSV results of rGO/$CuAlO_2$ nanocomposites, we infer that the oxidation current has a linear relationship with DA concentration, with a correlation coefficient of 0.9972, found to be better than that of $CuAlO_2$ (0.9921). Also, it clearly indicated that the rGO/$CuAlO_2$ nanocomposites have fast and highly sensitive response with variation in the concentration of DA when compared to $CuAlO_2$ which shows a gradual increase. The current response time of the rGO/$CuAlO_2$ nanocomposite-modified electrode was <5 s after the introduction of DA, indicating the oxidation of DA. Hence, the rGO/$CuAlO_2$ nanocomposites show excellent properties than $CuAlO_2$.

Further, the amperometric technique was involved to analyze the high sensitivity and low detection limits. The DA peak current was increased with DA concentration in the range of 9.2×10^{-8} to 1.6×10^{-7} M, as observed in the linear plot with a correlation coefficient of 0.9924 and 0.9976 by the $CuAlO_2$ nanostructure- and rGO/$CuAlO_2$ nanocomposite-modified electrodes (inset of Figure 8c,d), and the sensitivity was determined using the amperometric technique.[45,46] The response of current for the addition of each 100 nM is presented in Figure 8c,d. The response of steady-state current was obtained within 5 s at the sample interval of 180 s and an applied potential of 0.2 V. From these present reports, the low detection limit of 43 and 15 nM at an S/N = 3 for DA concentrations was obtained for the $CuAlO_2$ nanostructure- and rGO/$CuAlO_2$ nanocomposite-functionalized electrodes, which indicates high selectivity and good sensitivity toward DA. Comparison of rGO/$CuAlO_2$ nanocomposite-functionalized electrode with other electrodes is shown in Table 1.

Table 1. Comparison of the Analytical Performances of Various Modified Electrodes

electrode	pH	linear concentration	detection limit (nM)	refs
nitrogen-doped carbon nanofiber	7.0	1.0−200 μM	500	47
Au/graphene nanocomposite	7.0	0.5−411 μM	56	48
TiO_2−G/GCE	7.0	5−200 μM	200	49
G−Au film/GCE	6.0	5−1000 μM	186	50
BDD	7.0	5−100 μM	110	51
tiron/GCE	3.0	0.2−45.8 μM	70	52
PAYR/CPE	7.0	0.49−70.1 μM	160	53
rGO/$CuAlO_2$	7.2	9.2×10^{-8} to 1.6×10^{-7} M	15	this work

The reproducibility of the $CuAlO_2$ nanostructure- and rGO/$CuAlO_2$ nanocomposite-functionalized electrodes was estimated for 0−50 mM in the linear range of 9.2×10^{-8} to 1.6×10^{-7} M using CV measurements. Good reproducibility of the $CuAlO_2$ and rGO/$CuAlO_2$ biosensors at 1 μM response was noticed, and for 10 successive measurements, they were found to be 2.9 and 2.1%. The cathodic peak current decreased less than 3.1 and 2.4% for an interval of 4 h for $CuAlO_2$ nanostructure and rGO/$CuAlO_2$, indicating good stability of the biosensor. The functionalized electrode retained ∼97.8% response even after a week, realising the long-term stability, which comes from the strong interaction between rGO sheets and $CuAlO_2$. Therefore, we believe the rGO/$CuAlO_2$ nanocomposite sample has the capability of a biosensor in the clinical determination of DA because of its high selectivity and good sensitivity.

4. CONCLUSIONS

In summary, we have achieved the fabrication of rGO/$CuAlO_2$ nanocomposites as an electrode active material toward DA detection by synchronizing $CuAlO_2$ nanostructures and rGO sheets *via* a simple approach. The as prepared rGO/$CuAlO_2$ nanocomposite electrode revealed good catalytic activity toward oxidation of DA and low peak potential for low concentration of DA detection, compared to previously

https://dx.doi.org/10.1021/acsabm.0c00966
ACS Appl. Bio Mater. XXXX, XXX, XXX−XXX

reported electrodes. There are potential advantages of rGO/$CuAlO_2$ nanocomposites because they were prepared by a facile wet-chemical route which helps to increase the porous nature. Second, the modified electrode revealed higher analytical performance, successfully avoiding the interference of UA and AA, and exhibited enhanced selectivity, improved sensitivity, excellent linear response, low limit of detection, good stability, reproducibility, and repeatability. Third, we believe that the developed biosensor can work actively in real-time monitoring samples with good recoveries. Therefore, the rGO/$CuAlO_2$ nanocomposite-modified electrode has great ability to function as a next-generation clinical diagnostic for neurodegenerative disorders.

■ ASSOCIATED CONTENT

Supporting Information

The Supporting Information is available free of charge at https://pubs.acs.org/doi/10.1021/acsabm.0c00966.

Microspheres formed by numerous interconnected nanoparticles of average size ∼60 nm, enlarged view of the rGO peak positions (002) and (100) in the XRD pattern of rGO/$CuAlO_2$ nanocomposites, corresponding 2θ value at XRD peak appearing at 23.5 and 42.8° of graphene and the restoration of C−C (sp^2) bonding confirming the conversion of GO to rGO, and nitrogen adsorption−desorption isotherms and the corresponding pore size distribution of rGO (PDF)

■ AUTHOR INFORMATION

Corresponding Author

Thirumalairajan Subramaniam − *Department of Nano Science and Technology, Tamilnadu Agricultural University, Coimbatore 641003, India;* orcid.org/0000-0002-5694-2297; Phone: +9384534689; Email: sthirumalairajan@gmail.com; Fax: +91-422-6615524

Authors

Girija Kesavan − *Department of Physics, Dr. N.G.P. Arts and Science College, Coimbatore 641 048, India*

Ganesh Venkatachalam − *Electrodics and Electro Catalysis Division, CSIR-CECRI, Karaikudi 630 006, India;* orcid.org/0000-0001-8059-7043

Complete contact information is available at: https://pubs.acs.org/10.1021/acsabm.0c00966

Notes

The authors declare no competing financial interest.

■ ACKNOWLEDGMENTS

T.S. thankfully acknowledges the DBT-Ramalingaswami Re-entry Faculty Fellow scheme: 2018−2023, grant no. D.B. HRD/35/2006 date 19.11.2018 for funding this present work.

■ REFERENCES

(1) Phillips, P. E. M.; Stuber, G. D.; Heien, M. L. A. V.; Wightman, R. M.; Carelli, R. M. Subsecond Dopamine Release Promotes Cocaine Seeking. *Nature* **2003**, *422*, 614−618.

(2) Zare-Mehrjardi, H. R. Preparation of Modified Electrode using Toluidine Blue O and Molybdenum Schiff Base Complex for Detection of Dopamine in the Presence of Ascorbic Acid. *Anal. Bioanal. Electrochem.* **2018**, *10*, 52−63.

(3) Sajid, M.; Nazal, M. K.; Mansha, M.; Alsharaa, A.; Jillani, S. M. S.; Basheer, C. Chemically Modified Electrodes for Electrochemical Detection of Dopamine in the Presence of UA and AsA: A Review. *TrAC, Trends Anal. Chem.* **2016**, *76*, 15−29.

(4) Nagal, A.; Singla, R. K. Parkinson's Disease: Diagnosis, Therapeutics & Management. *WebmedCentral Pharm. Sci.* **2012**, *3*, WMC003670.

(5) Barsan, M. M.; Enache, T. A.; Preda, N.; Stan, G.; Apostol, N. G.; Matei, E.; Kuncser, A.; Diculescu, V. C. Direct Immobilization of Biomolecules through Magnetic Forces on Ni Electrodes via Ni Nanoparticles: Applications in Electrochemical Biosensors. *ACS Appl. Mater. Interfaces* **2019**, *11*, 19867−19877.

(6) de la Rica, R.; Stevens, M. M. Plasmonic ELISA for the Ultrasensitive Detection of Disease Biomarkers with the Naked Eye. *Nat. Nanotechnol.* **2012**, *7*, 821−824.

(7) Nezhad, M. R. H.; Tashkhourian, J.; Khodaveisi, J. Sensitive Spectrophotometric Detection of Dopamine, Levodopa and Adrenaline Using Surface Plasmon Resonance Band of Silver Nanoparticles. *J. Iran. Chem. Soc.* **2010**, *7*, S83−S91.

(8) Fu, X.; Tan, X.; Yuan, R.; Chen, S. A Dual-potential Electrochemiluminescence Ratiometric Sensor for Sensitive Detection of Dopamine Based on Graphene-CdTe Quantum Dots and Self-enhanced Ru (II) Complex. *Biosens. Bioelectron.* **2017**, *90*, 61−68.

(9) Reddy, S.; Xiao, Q.; Liu, H.; Li, C.; Chen, S.; Wang, C.; Chiu, K.; Chen, N.; Tu, Y.; Ramakrishna, S.; He, L. Bionanotube/Poly(3,4-ethylenedioxythiophene) Nanohybrid as an Electrode for the Neural Interface and Dopamine Sensor. *ACS Appl. Mater. Interfaces* **2019**, *11*, 18254−18267.

(10) Liu, A.; Wei, M. D.; Honma, I.; Zhou, H. Biosensing Properties of Titanatenanotube Films: Selective Detection of Dopamine in the Presence of Ascorbate and Uric Acid. *Adv. Funct. Mater.* **2006**, *16*, 371−376.

(11) Barsan, M. M.; Enache, T. A.; Preda, N.; Stan, G.; Apostol, N. G.; Matei, E.; Kuncser, A.; Diculescu, V. C. Direct Immobilization of Biomolecules through Magnetic Forces on Ni Electrodes via Ni Nanoparticles: Applications in Electrochemical Biosensors. *ACS Appl. Mater. Interfaces* **2019**, *11*, 19867−19877.

(12) Qiu, Z.; Yang, T.; Gao, R.; Jie, G.; Hou, W. An electrochemical ratiometric sensor based on 2D MOF nanosheet/Au/polyxanthurenic acid composite for detection of dopamine. *J. Electroanal. Chem.* **2019**, *835*, 123−129.

(13) Wiench, P.; González, Z.; Menéndez, R.; Grzyb, B.; Gryglewicz, G. Beneficial impact of oxygen on the electrochemical performance of dopamine sensors based on N-doped reduced graphene oxides. *Sens. Actuators, B* **2018**, *257*, 143−153.

(14) Yu, D.; Zeng, Y.; Qi, Y.; Zhou, T.; Shi, G. A novel electrochemical sensor for determination of dopamine based on AuNPs@SiO2 core-shell imprinted composite. *Biosens. Bioelectron.* **2012**, *38*, 270−277.

(15) Qiu, Z.; Yang, T.; Gao, R.; Jie, G.; Hou, W. An electrochemical ratiometric sensor based on 2D MOF nanosheet/Au/polyxanthurenic acid composite for detection of dopamine. *J. Electroanal. Chem.* **2019**, *835*, 123−129.

(16) Li, S.; Ma, Y.; Liu, Y.; Xin, G.; Wang, M.; Zhang, Z.; Liu, Z. Electrochemical sensor based on a three dimensional nanostructured MoS2 nanosphere-PANI/reduced graphene oxide composite for simultaneous detection of ascorbic acid, dopamine, and uric acid. *RSC Adv.* **2019**, *9*, 2997−3003.

(17) Feng, X.; Zhang, Y.; Zhou, J.; Li, Y.; Chen, S.; Zhang, L.; Ma, Y.; Wang, L.; Yan, X. Three-dimensional nitrogen-doped graphene as an ultrasensitive electrochemical sensor for the detection of dopamine. *Nanoscale* **2015**, *7*, 2427−2432.

(18) Li, S.; Ma, Y.; Liu, Y.; Xin, G.; Wang, M.; Zhang, Z.; Liu, Z. Electrochemical sensor based on a three dimensional nanostructured MoS2 nanosphere-PANI/reduced graphene oxide composite for simultaneous detection of ascorbic acid, dopamine, and uric acid. *RSC Adv.* **2019**, *9*, 2997−3003.

(19) Thirumalairajan, S.; Girija, K.; Ganesh, V.; Mangalaraj, D.; Viswanathan, C.; Ponpandian, N. Novel Synthesis of LaFeO3 Nanostructure Dendrites: A Systematic Investigation of Growth Mechanism, Properties, and Biosensing for Highly Selective

https://dx.doi.org/10.1021/acsabm.0c00966
ACS Appl. Bio Mater. XXXX, XXX, XXX−XXX

Determination of Neurotransmitter Compounds. *Cryst. Growth Des.* **2013**, *13*, 291−302.
(20) Anithaa, A. C.; Lavanya, N.; Asokan, K.; Sekar, C. WO3 nanoparticles based direct electrochemical dopamine sensor in the presence of ascorbic acid. *Electrochim. Acta* **2015**, *167*, 294−302.
(21) Wu, D.; Li, Y.; Zhang, Y.; Wang, P.; Wei, Q.; Du, B. Sensitive Electrochemical Sensor for Simultaneous Determination of Dopamine, Ascorbic Acid, and Uric Acid Enhanced by Amino-group Functionalized Mesoporous Fe3O4@Graphene Sheets. *Electrochim. Acta* **2014**, *116*, 244−249.
(22) Qian, T.; Yu, C.; Zhou, X.; Ma, P.; Wu, S.; Xu, L.; Shen, J. Ultrasensitive dopamine sensor based on novel molecularly imprinted polypyrrole coated carbon nanotubes. *Biosens. Bioelectron.* **2014**, *58*, 237−241.
(23) Gu, X.; Yue, J.; Chen, L.; Liu, S.; Xu, H.; Yang, J.; Qian, Y.; Zhao, X. Coaxial MnO/N-doped carbon nanorods for advanced lithium-ion battery anodes. *J. Mater. Chem. A* **2015**, *3*, 1037−1041.
(24) Feng, J.-J.; Guo, H.; Li, Y.-F.; Wang, Y.-H.; Chen, W.-Y.; Wang, A.-J. Single Molecular Functionalized Gold Nanoparticles for Hydrogen-Bonding Recognition and Colorimetric Detection of Dopamine with High Sensitivity and Selectivity. *ACS Appl. Mater. Interfaces* **2013**, *5*, 1226−1231.
(25) Kumar, M. K.; Prataap, R. K. V.; Mohan, S.; Jha, S. K. Preparation of Electro-rGO Supported Walnut Shape Nickel Nanostructures, and Their Application to Selective Detection of Dopamine. *Microchim. Acta* **2016**, *183*, 1759−1768.
(26) Tang, S.; Zhou, X.; Zhang, S.; Li, X.; Yang, T.; Hu, W.; Jiang, J.; Luo, Y. Metal-Free Boron Nitride Nanoribbon Catalysts for Electrochemical CO_2 Reduction: Combining High Activity and Selectivity. *ACS Appl. Mater. Interfaces* **2019**, *11*, 906−915.
(27) Balasubramanian, P.; Settu, R.; Chen, S.-M.; Chen, T.-W. Voltammetric sensing of sulfamethoxazole using a glassy carbon electrode modified with a graphitic carbon nitride and zinc oxide nanocomposite. *Microchim. Acta* **2018**, *185*, 396.
(28) Yang, T.; Chen, H.; Jing, C.; Luo, S.; Li, W.; Jiao, K. Using poly (m-aminobenzenesulfonic acid)-reduced MoS2 nanocomposite synergistic electrocatalysis for determination of dopamine. *Sens. Actuators, B* **2017**, *249*, 451−457.
(29) Thirumalairajan, S.; Mastealro, V. R. A novel organic pollutants gas sensing material *p*-type $CuAlO_2$ microsphere constituted of nanoparticles for environmental remediation. *Sens. Actuators, B* **2016**, *223*, 138−148.
(30) Hummers, W. S.; Offeman, R. E. Preparation of graphitic oxide. *J. Am. Chem. Soc.* **1958**, *80*, 1339.
(31) Thirumalairajan, S.; Girija, K.; Mastealro, V. R.; Subramanian, K. S. Enhanced ultrasensitive detection of ozone gas using reduced graphene oxide-incorporated $LaFeO_3$ nanospheres for environmental remediation process. *J. Mater. Sci.: Mater. Electron.* **2020**, *31*, 8933−8945.
(32) Bose, S.; Kuila, T.; Mishra, A. K.; Kim, N. H.; Lee, J. H. Dual role of glycine as a chemical functionalizer and a reducing agent in the preparation of graphene: an environmentally friendly method. *J. Mater. Chem.* **2012**, *22*, 9696−9703.
(33) Xia, Y.; Wang, J.; Xu, J.-L.; Li, X.; Xie, D.; Xiang, L.; Komarneni, S. Confined formation of ultrathin ZnO nanorods/rGO mesoporous nanocomposites for high-performance room-temperature NO_2 sensors. *ACS Appl. Mater. Interfaces* **2016**, *8*, 35454−35463.
(34) He, T.; Meng, X.; Nie, J.; Tong, Y.; Cai, K. Thermally Reduced Graphene Oxide Electrochemically Activated by Bis-Spiro Quaternary Alkyl Ammonium for Capacitors. *ACS Appl. Mater. Interfaces* **2016**, *8*, 13865−13870.
(35) Thirumalairajan, S.; Mastealro, V. R.; Escanhoela, C. A. In-depth understanding of the relation between $CuAlO_2$ particle size and morphology for ozone gas sensor detection at a Nanoscale level. *ACS Appl. Mater. Interfaces* **2014**, *6*, 21739−21749.
(36) Wu, X.; Xing, Y.; Pierce, D.; Zhao, J. X. One-Pot Synthesis of rGO/metal oxide Composites. *ACS Appl. Mater. Interfaces* **2017**, *9*, 37962−37971.
(37) Novoselov, K. S.; Fal'ko, V. I.; Colombo, L.; Gellert, P. R.; Schwab, M. G.; Kim, K. A roadmap for graphene. *Nature* **2012**, *490*, 192−200.
(38) Tate, J.; Ju, H. L.; Moon, J. C.; Zakutayev, A.; Richard, A. P.; Russell, J. Origin of p-type conduction in single-crystal $CuAlO_2$. *Phys. Rev. B: Condens. Matter Mater. Phys.* **2009**, *80*, 165206.
(39) Zou, Y. S.; Wang, H. P.; Zhang, S. L.; Lou, D.; Dong, Y. H.; Song, X. F.; Zeng, H. B. Structural, electrical and optical properties of Mg-doped $CuAlO_2$ films by pulsed laser deposition. *RSC Adv.* **2014**, *4*, 41294−41300.
(40) Santra, S.; Das, N. S.; Besra, N.; Banerjee, D.; Chattopadhyay, K. K. Graphene-Anchored p-Type CuBO2 Nanocrystals for a Transparent Cold Cathode. *Langmuir* **2017**, *33*, 9961−9971.
(41) Das, A. K.; Srivastav, M.; Layek, R. K.; Uddin, M. E.; Jung, D.; Kim, N. H.; Lee, J. H. Iodide-mediated room temperature reduction of graphene oxide: a rapid chemical route for the synthesis of a bifunctional electrocatalyst. *J. Mater. Chem. A* **2014**, *2*, 1332−1340.
(42) Wu, D.; Li, Y.; Zhang, Y.; Wang, P.; Wei, Q.; Du, B. Sensitive Electrochemical Sensor for Simultaneous Determination of Dopamine, Ascorbic Acid, and Uric Acid Enhanced by Amino-group Functionalized Mesoporous Fe3O4@Graphene Sheets. *Electrochim. Acta* **2014**, *116*, 244−249.
(43) Belaidi, F. S.; Civélas, A.; Castagnola, V.; Tsopela, A.; Mazenq, L.; Gros, P.; Launay, J.; Temple-Boyer, P. PEDOT-modified integrated microelectrodes for the detection of ascorbic acid, dopamine and uric acid. *Sens. Actuators, B* **2015**, *214*, 1−9.
(44) Moghadam, M. R.; Dadfarnia, S.; Shabani, A. M. H.; Shahbazikhah, P. Chemometric-assisted kinetic-spectrophotometric method for simultaneous determination of ascorbic acid, uric acid, and dopamine. *Anal. Biochem.* **2011**, *410*, 289−295.
(45) Yuan, D.; Chen, S.; Hu, F.; Wang, C.; Yuan, R. Non-enzymatic amperometric sensor of catechol and hydroquinone using Pt-Au-organosilica@chitosan composites modified electrode. *Sens. Actuators, B* **2012**, *168*, 193−199.
(46) He, J.; Qiu, R.; Li, W.; Xing, S.; Song, Z.; Li, Q.; Zhang, S. A voltammetric sensor based on eosin Y film modified glassy carbon electrode for simultaneous determination of hydroquinone and catechol. *Anal. Methods* **2014**, *6*, 6494−6503.
(47) Sun, J.; Li, L.; Zhang, X.; Liu, D.; Lv, S.; Zhu, D.; Wu, T.; You, T. Simultaneous determination of ascorbic acid, dopamine and uric acid at a nitrogen-doped carbon nanofiber modified electrode. *RSC Adv.* **2015**, *5*, 11925−11932.
(48) Huang, Q.; Lin, X.; Lin, C.; Zhang, Y.; Hu, S.; Wei, C. A high performance electrochemical biosensor based on Cu_2O−carbon dots for selective and sensitive determination of dopamine in human serum. *RSC Adv.* **2015**, *5*, 54102−54108.
(49) Josephine, D. S. R.; Babu, K. J.; Kumar, G. p. G.; Sethuraman, K. Titanium dioxide anchored graphene oxide nanosheets for highly selective voltammetric sensing of dopamine. *Microchim. Acta* **2017**, *184*, 781−879.
(50) Li, J.; Yang, J.; Yang, Z.; Li, Y.; Yu, S.; Xu, Q.; Hu, X. Graphene−Au nanoparticles nanocomposite film for selective electrochemical determination of dopamine. *Anal. Methods* **2012**, *4*, 1725−1728.
(51) Ekabutr, P.; Klinkajon, W.; Sangsanoh, P.; Chailapakul, O.; Niamlang, P.; Khampieng, T.; Supaphol, P. Electrospinning: A carbonized gold/graphene/PAN nanofiber for high performance biosensing. *Anal. Methods* **2018**, *10*, 874−883.
(52) Ensafi, A. A.; Taei, M.; Khayamian, T. Simultaneous Determination of Ascorbic Acid, Dopamine, and Uric Acid by Differential Pulse Voltammetry using Tiron Modified Glassy Carbon Electrode. *Int. J. Electrochem. Sci.* **2010**, *5*, 116−130.
(53) Zhou, Y.; Tang, W.; Wang, J.; Zhang, G.; Chai, S.; Zhang, L.; Liu, T. Selective determination of dopamine and uric acid using electrochemical sensor based on poly(alizarin yellow R) film-modified electrode. *Anal. Methods* **2014**, *6*, 3474−3481.

https://dx.doi.org/10.1021/acsabm.0c00966
ACS Appl. Bio Mater. XXXX, XXX, XXX−XXX